Ocean tracer distributions

Part I. A preliminary numerical experiment

By WILLIAM R. HOLLAND, *Geophysical Fluid Dynamics Laboratory/NOAA, Princeton University, Princeton, N.J. 08540, USA*

(Manuscript received January 20, 1971)

ABSTRACT

A numerical experiment has been carried out to determine the three-dimensional distributions of dissolved oxygen and radiocarbon as well as the fields of temperature, salinity, and velocity in an ocean driven by wind and thermohaline processes. The aim in this preliminary calculation was to test the usefulness of a tracer model for studying the origin of water masses in the sea and to provide a framework for looking further into the nature of the sources, age, and circulation of the abyssal ocean.

Much of our knowledge about circulation patterns and mixing in the sea has come from examining the distribution of properties in simplified one and two dimensional models. In this investigation tracer studies are extended to three dimensions using a numerical model of the ocean circulation of the kind described by Bryan (1969). With a given set of parameters and boundary conditions governing the model ocean, a calculation is made to predict the distributions of four "tracers", temperature, salinity, dissolved oxygen, and radiocarbon, as well as the structure of the circulation. Based upon this first experiment some important conclusions can be made regarding those features necessary in any model to satisfactorily account for observed distributions.

Part I describes the physical model and its numerical analogue as well as the numerical techniques used in finding a steady state. The results of an experiment with tracer eddy diffusivities $K = 1$ cm^2/sec (vertical) and $A_H = 5 \times 10^7$ cm^2/sec (horizontal) are examined in some detail to understand the time scales involved for the deep sea as well as the shallower regions. The patterns of flow and the distributions of the four tracers are related to each other by determining the roles of diffusion, advection, and decay processes in the model. Comparisons are made between observed and predicted surface fluxes of heat and evaporation minus precipitation in order to ascertain the effect of the boundary conditions on the nature of the distributions.

These results suggest the direction further studies should take in constructing realistic models of the ocean. Calculations with smaller diffusivities and other boundary conditions are underway and will be reported in Part II.

1. Introduction

The distributions of various conservative and non-conservative properties, such as temperature, salinity, oxygen, and radiocarbon, have been used extensively to understand the patterns of motion in the sea. Although oceanographers are beginning to do more than collect scattered and infrequent direct measurements of the velocity field, it is still true that most knowledge about oceanic motions comes indirectly from temperature and salinity measurements and from measurements of other assorted chemical constituents of sea water. Such indirect techniques include the calculation of geostrophic currents, the computation of heat, salt, and oxygen budgets, the use of reservoir and continuous models including various tracers, and the determinations of age or rate of flow based upon decay rates of radioactive constituents of sea water. All of these have provided and will continue to provide an important and independent approach to understanding the motions and mixing in the ocean.

In the last few years the geochemists have developed techniques for adding further interesting oceanic tracers to those already available and, as these data become more extensive, they will impose further constraints on the models that are constructed for studying the ocean. It is useful then to provide a framework into which these new data as well as the more extensive traditional data can be fitted to form a quantitative as well as a qualitative picture of how the ocean operates. This is one of the aims of this study.

There are many fruitful approaches to constructing models which make use of the known distribution of tracers to understand ocean movements. Among these are two categories which may be called (*a*) continuous models and (*b*) box models. Wyrtki (1962), Munk (1966), Arons & Stommel (1967), Kuo & Veronis (1970) and many others have examined simple continuous models governed by diffusive, advective, and decay processes to gain insight into both vertical and horizontal mean motions and to evaluate the strength of turbulent mixing in the ocean. Craig (1957), Broecker et al. (1960), Bolin & Stommel (1961), and Keeling & Bolin (1967, 1968), among others, have divided the oceans into a limited number of boxes or reservoirs to ascertain some of the gross features of the circulation and mixing based upon budget calculations for various tracers.

The present investigation, in a strict sense, belongs to the discontinuous category in that solutions are obtained for a set of finite difference equations. Each grid point may be considered the center of a tiny cell or reservoir, each with its tracer concentrations and with advective and diffusive fluxes through the faces of the cell. Because of the large number of cells, however, the finite difference system is a good approximation to the set of differential equations and it is appropriate to think in terms of the continuous equations.

The main difference between the present investigation and the ones mentioned above is not the continuous or discontinuous nature of the model but rather that this model is fully three-dimensional and allows for the mutual adjustment of the velocity and density (T and S) fields. The amount and manner of sinking at high latitudes to fill the deep sea is to be found from the calculation, and the various modes of transport of the several tracers, both vertically and horizontally, are to be determined. This is a different approach from the continuous models mentioned above which fix the nature of the circulation and then find the tracer distributions which are consistent with it.

Keeling & Bolin (1968) have pointed out in connection with box models that "it hardly seems feasible to increase the spacial resolution by using a larger number of reservoirs without introducing the constraints in the hydrodynamic and thermodynamic equations that govern the motions of the oceans". This in fact is what is being done in this study. Within the context of a 3-d numerical model the hydrodynamic, thermodynamic, and tracer equations are solved simultaneously, mutually constraining one another through the interaction terms in the equations. The aim is then to understand which factors are important in determining the major features of the large scale tracer distributions as a key to understanding the major features of the oceanic circulation.

2. Description of the model

The model ocean is a simple one. The basin is bounded by meridional walls separated by 45° of longitude and by a northern wall located at latitude 64.2° N. Symmetry is assumed about the equator so that calculations are done only for the northern half of the ocean, that is from 0° to 64.2° N. Bottom topography is not included in this first study; the ocean floor is flat and located at a depth of 4 000 meters.

The ocean is driven by the wind and by a north–south density distribution imposed at the sea surface by the boundary conditions on temperature and salinity. The surface conditions are independent of time and, for the parameters used in this study, the tracer and velocity distributions become steady after an extensive integration. It is this steady state which will be examined.

The equations which govern the concentration of various tracers are based upon the principle of dynamic equilibrium which is discussed in *The Oceans* (Sverdrup, Johnson & Fleming, 1942, p. 160). In words, the local time rate o change of each tracer concentration is equal to the change due to diffusive processes plus the change due to advective processes plus the change due to decay processes, if any. The tracer equations then all have the form

$$s_t = \mathcal{D}s - \mathcal{L}s - \mathcal{R}(s) \qquad (2.1)$$

where s is the tracer concentration. The diffusion operator $\mathcal{D}$, the advection operator $\mathcal{L}$ and the source-sink function $\mathcal{R}$ are defined and discussed below.

Let

$$m = \sec \varphi$$
$$n = \sin \varphi$$
$$u = a\dot{\lambda}/m$$
$$v = a\dot{\varphi}$$

where a is the radius of the earth, φ is latitude, λ is longitude, and u and v are the eastward and northward components of velocity. Then, if μ is some scalar quantity, the operators $\mathcal{D}$ and $\mathcal{L}$ are defined

$$\mathcal{D}\mu = K\mu_{zz} + \frac{A_H}{a^2}\,[m^2\mu_{\lambda\lambda} + m(\mu_\varphi/m)_\varphi] \quad (2.2)$$

and

$$\mathcal{L}\mu = \frac{m}{a}\,[(\mu u)_\lambda + (\mu v/m)_\varphi] + (\mu w)_z \quad (2.3)$$

Here z is the depth (measured positive upward), w is the vertical velocity, and K and A_H are coefficients of vertical and horizontal eddy diffusion for the tracers.

Local convective overturning in the ocean involves processes of such a small scale that they cannot be resolved by the numerical grid. Therefore convection is handled implicitly by the procedure described in Bryan & Cox (1968). At each time step the vertical density structure is examined for stability. If an unstably stratified region is found, the tracers are mixed vertically there so that the vertical gradients of T, S, O_2, and C^{14} vanish. The total amounts are conserved in this process; the tracers are merely redistributed vertically to bring the unstable region to a neutral condition. This *convective mixing* process may be thought of as providing a vertical flux in addition to the diffusive flux, $-Ks$, based upon a constant K. Alternatively one can consider K to be constant for stable stratification but to become infinite in unstable regions.

While the diffusion and advection terms in equation (2.1) represent an internal readjustment of the tracer concentrations, the decay term $\mathcal{R}(s)$ and the boundary conditions which supplement equation (2.1) describe sources and sinks of the tracers and play a fundamental role in determining the overall distributions. Thus it is appropriate that these be discussed in some detail for each tracer treated in this study.

The term $\mathcal{R}(s)$ represents *internal* sources and sinks for any given tracer. For temperature and salinity there are none; $\mathcal{R}(T)$ and $\mathcal{R}(S)$ are identically zero. Except in the thin euphotic zone where photosynthesis may lead to a production of oxygen, biological processes that influence the oxygen content always lead to a consumption of oxygen. Thus $\mathcal{R}(O_2)$ represents a sink function. Little is known about variations in the rates of oxygen consumption in the horizontal but Sverdrup & Fleming (1941) and Riley (1951), among others, have made estimates of the vertical structure of $\mathcal{R}(O_2)$. Wyrtki (1962), in an interesting study of the relationship of the oxygen minimum to ocean circulation, pointed out that an exponential curve gave a reasonable fit to Riley's data in the upper 1 500 m. Models based upon deep data [Arons & Stommel (1967), Munk (1966)] use an $\mathcal{R}$ value of about 0.002 (ml/l) year^{-1} in the abyssal ocean which is not inconsistent with Riley's results. All of these pieces of information can be accommodated in a simple form for $\mathcal{R}(O_2)$

$$\mathcal{R}(O_2) = A + B \exp(-\gamma z)$$

where $A = 0.635 \times 10^{-10}$ (ml/l) sec^{-1}, $B = 100 \times 10^{-10}$ (ml/l) sec^{-1}, and $\gamma = 0.350 \times 10^{-2}$ m^{-1}. Variations with latitude and longitude are ignored in the expectation that horizontal variations in the oxygen distribution will then reflect the important effects of the circulation pattern. Eventually, however, it will be necessary to investigate the distribution of these internal sources and sinks and a model like this one will provide a useful tool for doing so.

The form of the function $\mathcal{R}$ for a radioactive tracer with no other sources and sinks than its natural radioactive decay is a simple one. For radiocarbon it may be written

$$\mathcal{R}(C^{14}) = \beta C^{14}$$

where $\beta = 3.93 \times 10^{-12}$ sec^{-1}, based upon a half-life of 5 568 years. This is the decay law used in this study. Two difficulties should be kept in mind however in comparing these data with oceanic measurements of radiocarbon (Craig, 1969): firstly, particulate fluxes of radiocarbon which have been ignored here may be of importance; secondly "radiocarbon measurements" are actually of the isotope ratio C^{14}/C^{12} and not the absolute concentration of C^{14} itself.

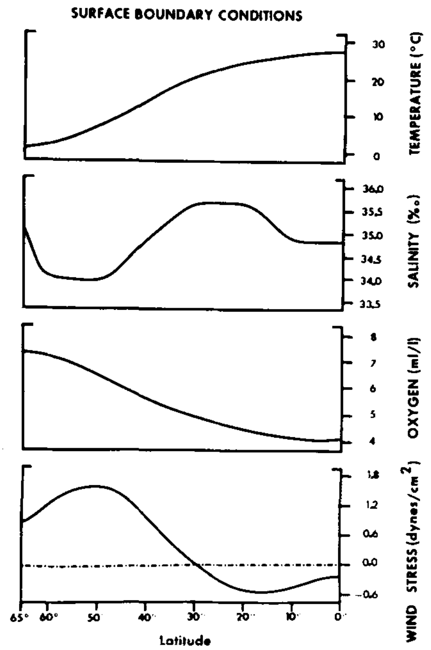

Fig. 1. The boundary conditions imposed at the surface of the model ocean. The temperature, salinity, dissolved oxygen, and eastward wind stress are shown as functions of latitude. These boundary conditions are assumed to be independent of longitude.

Thus for direct comparison between ocean and model, the ocean data must be corrected for C^{12} variations before conclusions can be reached about how well model distributions represent oceanic ones. Craig (1969) examines these questions in some detail using real data from the Pacific. In any event, as suggested above for oxygen consumption, the numerical model can in future be a useful tool for *determining* the internal sources and sinks of radiocarbon rather than specifying them from the inadequate data presently available.

The boundary conditions that accompany equation (2.1) are (*a*) the tracer distributions have zero normal derivative at the bottom of the model ocean and at its east, west, and north walls; (*b*) the distributions are symmetrical about the equator; and (*c*) the surface values are given functions of latitude. Conditions (*a*) and (*b*), together with the velocity boundary condition of zero mass flux through all of the bounding surfaces, result in there being no fluxes of heat, salt, oxygen or radiocarbon through the bottom or across the sides of the basin and the equator. The fluxes across the surface of the ocean however are quantities to be determined; they must be consistent with the internal distributions and dynamics and with boundary conditions (*c*).

The surface values of temperature, salinity, oxygen, and zonal wind stress used in this study are shown in Fig. 1. They are determined by zonal averages of real data from both hemispheres with one important modification; the salinity at the northern end of the basin has been increased somewhat to represent North Atlantic conditions rather than the average of all high latitude data where the Southern Ocean predominates. While the surface temperature and oxygen data are more or less symmetrical about the equator the salinity is quite different at high northern and southern latitudes, particularly in the Atlantic. This is one of the obvious difficulties in treating a simplified model. More realistic boundary conditions and geometry will be necessary to simulate distributions like those found in any of the actual ocean basins.

The surface radiocarbon values present a special problem. The C^{14} distributions are not only highly asymmetric about the equator, but in addition there is far less data available than for the other three tracers. It was decided therefore in this first calculation to choose a simple boundary condition: the surface has a uniform concentration of radiocarbon, C_s^{14}. Then since decay processes give rise to smaller concentrations of C^{14} in the interior of the ocean, the apparent age of the water there, with respect to a reference of zero age for the surface water, will be given by

$$T_a = \beta^{-1} \log (C_s^{14}/C^{14})$$

This quantity is a useful one for displaying radiocarbon concentrations.

The momentum and continuity equations, together with the equation of state and appropriate boundary conditions, complete the set of partial differential equations to be solved. The numerical model is similar to that of Bryan & Cox (1968), and the numerical equations and method of integrating them as an initial value problem have been fully discussed by Bryan (1969). The reader is directed to those papers if he is interested in details of the numerical model. In this investigation the time integration approach has not always been followed and various iterative techniques have been used to speed the convergence to a steady state.

The model ocean is assumed to be hydrostatic and the Boussinesq approximation is made. Further the vertical and horizontal mixing of momentum by scales smaller than grid size is represented by eddy diffusion with constant coefficients. Then the momentum and continuity equations become

$$u_t + \mathcal{L}u - 2\Omega nv - mnuv/a = -\frac{m}{a}\left(\frac{p}{\varrho_0}\right)_\lambda + F^\lambda \quad (2.4)$$

$$v_t + \mathcal{L}v + 2\Omega nu + mnu^2/a = -\frac{1}{a}\left(\frac{p}{\varrho_0}\right)_\varphi + F^\varphi \quad (2.5)$$

$$\varrho g = -p_z \quad (2.6)$$

$$w_z + \frac{m}{a}[u_\lambda + (v/m)_\varphi] = 0 \quad (2.7)$$

Here Ω is the rotation rate of the earth, p is the pressure, ϱ is the density, and F^λ and F^φ include the effects of the turbulent diffusion of momentum (Saint-Guily, 1956):

$$F^\lambda = A_V u_{zz} + \frac{A_M}{a^2}[m^2 u_{\lambda\lambda} + m(u_\varphi/m)_\varphi + (1 - m^2n^2)u - 2nm^2 v_\lambda] \quad (2.8)$$

$$F^\varphi = A_V v_{zz} + \frac{A_M}{a^2}[m^2 v_{\lambda\lambda} + m(v_\varphi/m)_\varphi + (1 - m^2n^2)v + 2nm^2 u_\lambda] \quad (2.9)$$

where A_V and A_M are the vertical and horizontal eddy viscosities. The values of A_V and A_M are 10 cm²/sec and 5×10^8 cm²/sec respectively, somewhat larger than the eddy diffusivities for the tracers. The tracer equations and momentum equations are coupled by the velocity terms in (2.1) but also by an equation of state of the form

$$\varrho = \varrho(T, S, p) \quad (2.10)$$

A convenient formula for (2.10) given by Eckart (1958) has been used in this study.

The boundary conditions on velocity at the north, east, and west walls are that $u = v = 0$ there and the symmetry condition at the equator requires that $v = 0$, $u_\varphi = 0$ there. At the top and bottom of the ocean $w = 0$ and therefore there is no mass flow in or out of the basin. The surface wind stress, assumed to be entirely zonal, is equal to the diffusive flux of momentum downward so that $\varrho_0 A_V u_z = \tau^w$ and $\varrho_0 A_V v_z = 0$. At the bottom of the ocean a simple stress law has been used in this study: $\tau_B^\lambda/\varrho_0 = -C_D u$ and $\tau_B^\varphi/\varrho_0 = -C_D v$ where τ_B^λ and τ_B^φ are the eastward and northward bottom stresses and C_D is the drag coefficient. The value of C_D (4×10^{-5} m/sec) was chosen so that bottom friction played only a minor role in the overall momentum and vorticity balances, but it was retained to help damp oscillatory motions which occurred early in the numerical integration.

Since the general nature of the finite difference formulation has been discussed in detail by Bryan (1969), here the discussion will be restricted to the specific features and techniques of this calculation. The study was begun as a time integration of the equations on a three-dimensional network of points which has 18 grid points in the zonal (λ) direction, 24 grid points in the meridional (φ) direction, and 7 grid points in the vertical. The distribution of points was not uniform but had a greater concentration near the lateral boundaries and near the upper surface. The lateral spacing near the walls was about 150 km and in the interior about 370 km. The vertical spacing varied from 120 m near the surface to 1 600 m in the deep ocean. Time integration, relaxation and extrapolation techniques all were employed to approach a steady state.

Since the focus of interest in this study was on the distribution of tracer properties and their vertical distributions were to be examined in detail, the vertical resolution was refined to a total of 19 layers, with vertical grid point spacing varying from 20 m at the surface to 400 m in the deep sea. The previous solution was interpolated onto the new grid and the time integration begun again.

The very long time scales associated with diffusion into the deep sea and with the radioactive decay of C^{14} made it clear, however, that a straight forward time integration of the equations was impossibly costly in computer time. A variety of iterative techniques were tested and used, but two of them proved especially useful in coping with the long term trends. The first was an extrapolation technique used in conjunction with time integration of the equations. After a time integration of some length $t_2 - t_1$ (typically 5 or 10 years of ocean time), the trends in T, S, O_2, and C^{14} at each grid point were used to predict new tracer fields, that is

$$s^3 = s^2 + \alpha(s^2 - s^1)$$

where s^3 denotes the new tracer distribution and s^1 and s^2 are the distributions at times t_1 and t_2. The new fields were then used as initial values for further time integration. Various extrapolation constants α were used, varying from conservative values of one to values as large as twenty. Thus it was possible to make a leries of linear forward extrapolations in time of sengths $\alpha(t_2 - t_1)$, with values as large as 200 years being used.

The second iterative technique was the Gauss-Seidel relaxation method (Todd, 1962) also known as the method of successive displacements, which was used to solve the time-independent tracer equations, holding the velocity field fixed during the process. Equation (2.1), with the local time derivative equal to zero, is a three-dimensional elliptic equation with non-constant coefficients which is solved subject to the imposed boundary conditions. Convergence was quite rapid, compared to time integration, and the new tracer fields were then used as initial data for further time-dependent integration.

These iterative techniques, coupled with time integration, led to a much more rapid approach to a steady state solution than straightforward time integration. Following a lengthy sequence of such operations the deep sea, as well as the rest of the basin, was brought into near balance as shown by examining the balance of terms in the tracer equations (see for example Fig. 17). The calculation was completed by a time integration of 50 years to examine the nature of any residual time dependent behavior.

3. Patterns of flow

Before the steady distributions of tracers are examined it is useful to look into the nature of the circulation pattern to assess the role played by advective processes. As a first step in

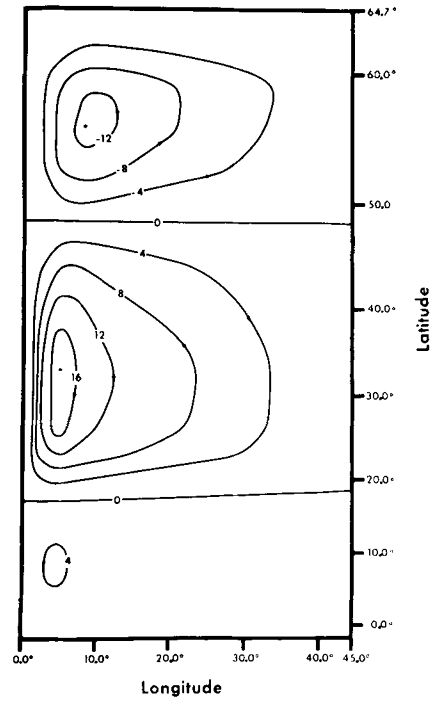

Fig. 2. The horizontal transport stream function. The unit are 10^6 m³/sec.

understanding the circulation, the volume transports in each of the three planes are calculated. For example, the continuity equation (2.7) may be integrated with respect to depth and the boundary conditions on w applied to find

$$\bar{u}_\lambda + (\bar{v}/m)_\varphi = 0$$

where $\overline{(\ )} = \int_{-H}^{0} (\ )\,dz$

If ψ is defined such that

$$\psi_\varphi = -a\bar{u}, \quad \psi_\lambda = a\bar{v}/m$$

then ψ is the volume transport stream function in the horizontal plane (Fig. 2). Similarly equation (2.7) may be integrated in the λ or the φ direction to find transport stream functions in the meridional-vertical plane or the zonal-vertical plane respectively. These are shown in Figs. 3 and 4 where the units are millions of cubic meters per second.

The horizontal transport pattern has three

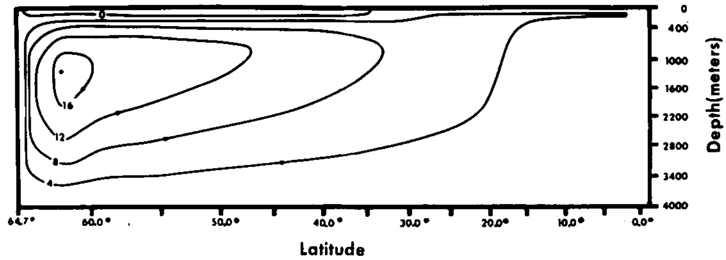

Fig. 3. The meridional transport stream function. The contour interval is four Sverdrups (one Sverdrup equals 10^6 m^3/sec).

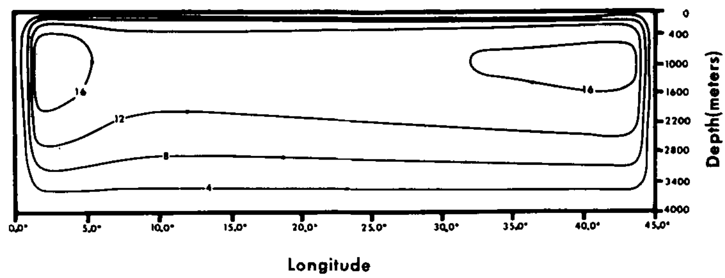

Fig. 4. The zonal transport stream function. The units are 10^6 m^3/sec.

gyres, each of which coincides well with its region of appropriate sign of the wind stress curl. The central subtropical gyre has a northward flowing western boundary current with a total transport of 18 million m^3/sec. That figure is well predicted by the Sverdrup (1947) analysis, if his equations are integrated from the eastern boundary, indicating there is no important contribution in this model by inertial recirculation as found by Veronis (1966). In fact, for the horizontal eddy viscosity used in this study ($A_m = 5 \times 10^8$ cm^2/sec) the western boundary current is strongly frictional, the transport is nearly symmetrical about the center of each gyre, and the Munk theory (1950) satisfactorily explains the horizontal transport pattern. There are at least two reasons for the small transport value of 18 million m^3/sec First the ocean is too narrow, only 45° of longitude, compared with about 65° for the North Atlantic and 90° for the North Pacific. Second as mentioned above the nonlinear terms are not important in the western boundary current so that there is no inertial enhancement there as discussed by Veronis (1966). Finally it should be kept in mind that bottom topography, which may have important effects on the transport, has been neglected.

The meridional volume transport, which is perhaps the most interesting of the three transports, is shown in Fig. 3. At the northern end of the basin there is a relatively narrow sinking region with southward flow below 1 000 m. South of 50° N a more or less uniform upward transport connects the deep flow with a northward return flow in the shallow water above a depth of about 500 m. The total transport is about 17 million m^3/sec, the same order as the horizontal transport. Near the equator there is a secondary very shallow gyre with southward flow at 200 m and northward flow above at a depth of 50 m or so. This equatorial flow pattern, which was noted by Bryan & Cox (1967), is driven by the local wind system and may be associated with the equatorial undercurrent.

The zonal transport is shown in Fig. 4. Again strong vertical transports are found near the walls, with upwelling near the western boundary and an equally strong downwelling near the eastern wall. The transport in the interior shows no tendency for rising or sinking motions in this north-south integral. It should be kept

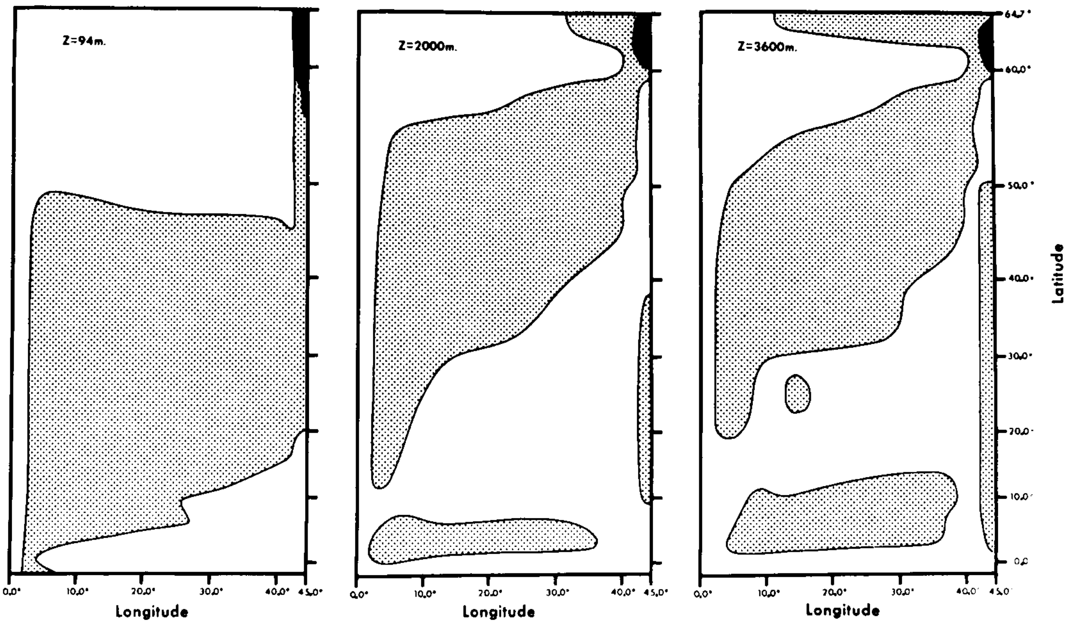

Fig. 5. The patterns of vertical motion at three levels in the ocean. The dotted regions indicate downward motion and the clear regions indicate upward motion. The black area shows regions of very large downward flow (on the order of 100 times the interior values). The three maps shown are at 94 m, 2 000 m, and 3 600 m.

in mind however that this east–west picture is an average over the three gyres found in Fig. 2 and at any given latitude there may be a quite different pattern of flow.

As an aid to putting together a more comprehensive picture of the circulation pattern, it is useful to look at the velocity components themselves in certain sections. In particular the patterns of rising and sinking motion are shown by maps of the vertical velocity field at three depths in the basin in Fig. 5. Upward motion is indicated by the unshaded regions and downward motion by the shaded ones. The very dark regions are regions of very strong downward motion. Two important features stand out immediately. First there is a very strong sinking region at all depths in the north–east corner of the basin. This appears to be the major "pipeline" from shallow to abyssal depths in the model and is the major contributor to the northern boundary sinking in Fig. 3 and the eastern boundary sinking in Fig. 4. Secondly the region adjacent to the western boundary is one of rising motions at all depths, suggesting that the uniform rising motion south of 50° N shown in Fig. 3 has in fact a major contribution near the western boundary as indicated by the upwelling there in Fig. 4. Thus the abyssal ocean seems to be fed by a source of limited geographical extent in the northeast corner and has a sink more or less uniformly distributed along the western boundary. The interior rising and sinking motions are not negligible because of their much greater area but they are much less intense. It should be noted that these boundary regions of intense vertical motion are represented by relatively few grid points and their detailed nature needs to be examined by greater resolution there in future experiments, but it is not thought likely that the gross picture will be altered much.

The manner in which these sources and sinks are connected by horizontal circulations is shown in Figs. 6 and 7. Fig. 6 shows Mercator maps of the horizontal velocity vectors at two horizontal levels, 52 m and 1 800 m. The shallow case shows a strong western boundary current between 20° and 40° N, with a broad diffuse flow toward the northeast, north of 40° N. At the equator a relatively intense eastward flowing undercurrent, the Cromwell Current in this model, is found. At 1 800 m the horizontal velocity vectors indicate a flow away from the source near the northeast corner in an intense

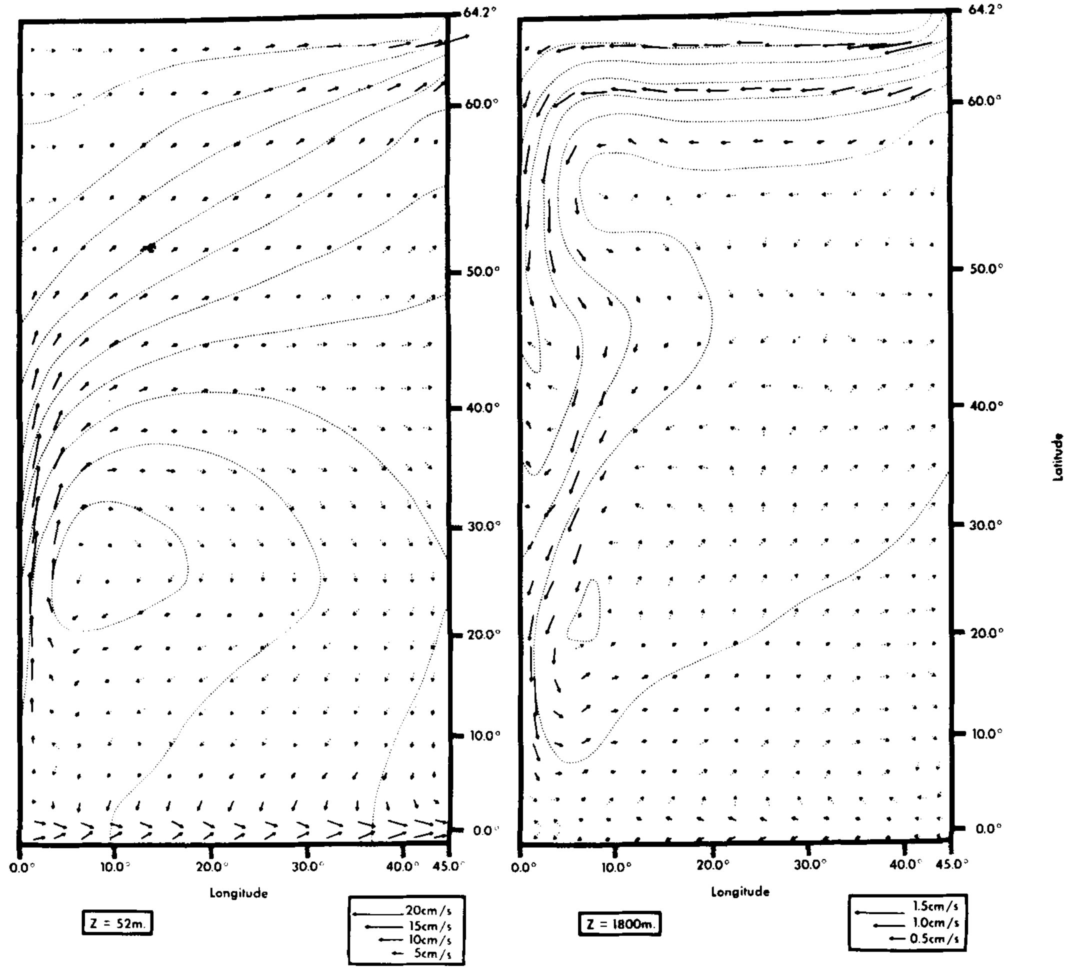

Fig. 6. The horizontal velocity vectors at two depths, 52 and 1 800 meters. Also shown are the lines of constant pressure (isobars), indicating the highly geostrophic nature of the flow except near the equator. Note the different velocity and pressure contour scales used at each level. Dashed arrow shafts have been added to vectors whose lengths are less than the size of the arrowhead to show more clearly their directions.

westward flowing boundary current. This current turns southward when it meets the western boundary and penetrates nearly to the equator as a distinct stream. This southward flowing western boundary current was suggested by Stommel (1957) and measured by Swallow and Worthington (1961) in the western North Atlantic.

Plotted also in Fig. 6 are lines of constant pressure which indicate that the flow is strongly geostrophic. Thus the pressure field serves as an ideal indicator of the direction and magnitude of flow, except in the vicinity of the equator where the geostrophic assumption breaks down.

Fig. 7 shows the relative pressure fields at several different depths to get a feel for the vertical structure of the horizontal circulation. The flow is clockwise around highs and counterclockwise around lows so that in the upper layers, as indicated by the isobaric maps at 79 m and 600 m, the flow originates near the western boundary and flows northeastward. Note the change in intensity of flow as indicated by changes in the pressure contour interval, $\Delta p/\varrho_0$. The velocities at 600 m are more or less in the same direction as those at 79 m but there is a factor of 5 reduction in intensity.

The 1 000 m map shows a transition be-

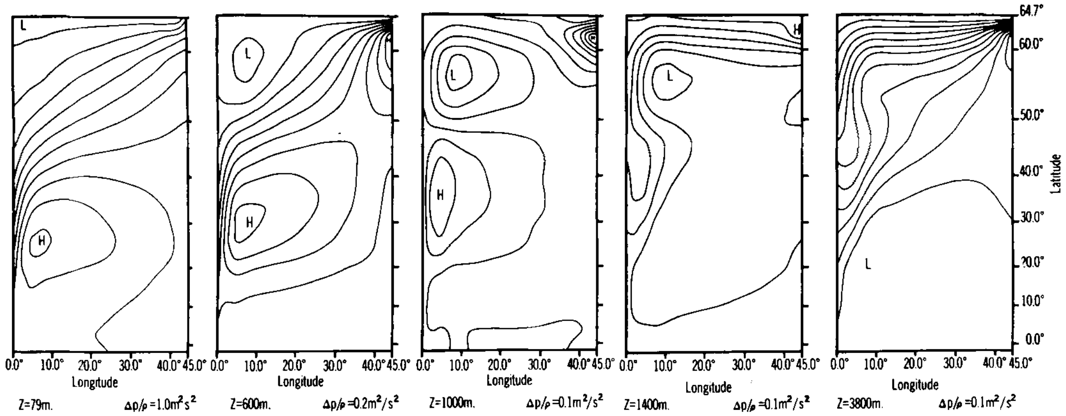

Fig. 7. The pressure field at five levels in the ocean. Centers of low and high pressure are denoted by L and H respectively. The contour interval, $\Delta p/\varrho_0$, is given below each map. Because of the highly geostrophic nature of the flow (except within about 5° of the equator) the isobars indicate very closely the direction of flow, which is clockwise around highs and counterclockwise around lows. Note the changes in intensity of flow at the various levels as indicated by changes in the pressure gradients.

tween the behavior of the shallow water, noted above, and the behavior of the deep water. The weak low pressure cell present at 600 m is further from the northwest corner and is more intense at 1 000 m, indicating a beginning of flow reversal that shows up at 1 400 m as a westward flowing current near the northern boundary and as a western boundary under-current flowing toward the south. This deep pattern of flow persists to the bottom of the ocean with some tendency for stronger velocities near the bottom.

Thus the patterns of flow found in this calculation have a simple but interesting structure, particularly in the way the abyssal circulation is fed from above in the northeast corner and returns water to the shallow layers as an upwelling of deep water along the entire western boundary. It appears that much of the deep ocean beyond the boundary current regions may be bypassed by this circulation in contrast to the abyssal circulation models studied by Stommel & Arons (1960) and to the assumed circulation in the recent model of Kuo & Veronis (1970). As is to be expected, these horizontal and vertical circulations have an important and in some parts of the model a dominant effect upon the distribution of tracers.

4. Tracer distributions

There are four factors which determine the steady tracer distributions in this study: (1) advective processes, which are governed by the patterns of motion discussed in the previous section; (2) diffusive processes, characterized by constant values of the horizontal and vertical eddy diffusivities, A_H and K (which are 5×10^7 cm²/sec and 1.0 cm²/sec respectively); (3) convective mixing in the presence of unstable density gradients; (4) decay processes. The equilibrium distributions brought about by the balance of these processes will be discussed qualitatively here. A quantitative examination of the balance of terms in tracer equation (2.1) will be made in the next section with particular attention paid to comparisons between model data and real ocean data.

Figures 8–11 show the horizontal distributions of T, S, O_2, and C^{14} at two depths in the model ocean. In Fig. 8 the temperature at 79 m is found to be still strongly influenced by the surface boundary condition shown in Fig. 1. The constant temperature contours are oriented in the east–west direction although near the western boundary the effect of the upwelling cold water is apparent. At 1 800 m the temperature field also reflects the advective pattern with colder water near the western boundary and a warm pool in the "Sargasso Sea" of the model. In the northeast corner the local downwelling brings slightly warmer water from above. The most striking feature of the deep temperatures (and the other tracers as we shall find) is the small range of variation there. The deep waters are rather homogeneous, showing less variation than is found in any of the real ocean basins. The reasons for this will be discussed in section 5.

Horizontal maps of the salinity distribution are shown in Fig. 9. The distribution at 79 m, like the temperature field, shows a strong resemblance to the applied surface conditions, particularly along the eastern side of the basin. Near the western boundary, northward advection by the "Gulf Stream" and upward motion there tend to smooth out the maximum at 23° N and the minimum at 55° N imposed by the boundary conditions. The 1 800 m map has an intermediate salinity of about 34.68 ‰ over much of the basin, but the downwelling in the northeast corner brings fresher water to this level. Again the homogeneous nature of the deep water is apparent; the salinity varies by only a few hundredths of a part per thousand in the deep water.

Dissolved oxygen distributions are shown in Fig. 10. The surface waters of the ocean are very nearly saturated with oxygen but the saturation value depends strongly on temperature. Thus, as shown in Fig. 1, the surface concentration varies from 4.1 ml/l near the equator to 7.3 ml/l at the northern end of the basin. The distribution at 79 m reflects the advective pattern as did the temperature and salinity. Near the western boundary there are relatively low values of oxygen concentration reflecting the northward advection from the equatorial minimum. Examination of the layers below 79 m shows a continued decrease down to about 200 m so that upwelling near the western boundary also contributes oxygen poor water to the surface layers there. The upward tilt of the isolines of oxygen, as well as those of temperature and salinity, near the western edge of the basin will be seen more clearly in the east-west sections which are examined later. At 1 800 m the oxygen concentration decreases from north to south by about 0.4 ml/l. Since the depth is below the oxygen minimum there are relatively high values near the western boundary due to upwelling of oxygen-rich water from below and due to the southward flowing undercurrent there. At this level a minimum value is found at the equator near the eastern boundary, suggesting that this point is the furthest removed from the surface sources of deep water.

Radiocarbon distributions are shown in Fig. 11. The quantity contoured in the diagrams is the "apparent age" (in years) with a reference of zero age for the surface waters (which are considered to have a constant concentration C_s^{14}). Thus the radiocarbon age at any point in the basin relative to the surface waters is defined by

$$T_a = \frac{1}{\beta} \log_e (C_s^{14}/C^{14})$$

where β is the decay constant based upon a half life of 5 568 years, and C^{14} is the radiocarbon concentration at the given point. If the concentration is everywhere normalized such that $C_s^{14} = 1.0$ then $\delta C^{14} = (C_s^{14} - 1.0) \times 1\,000$ will give the per mil decrease in radiocarbon concentration. Note that these per mil values are not directly comparable to those cited for example by Broecker et al. (1960) or by Bien et al. (1965) because a different reference level has been used.

The C^{14} concentrations, i.e. the ages, at 79 m again show the effect of the rising motion along the western boundary and also suggest that upwelling occurs near the southeast corner of the basin. The model ocean, even at this shallow depth, has ages greater than 60 years. The deep water ages on the 1 800 m map show "new" water near the northern boundary, where rapid vertical mixing takes place, and a steady increase in age toward the south. A maximum age of 150 years is found at the equator on the eastern side of the basin, confirming the suggestion based on oxygen data that the oldest water in the basin resides there.

North-south sections (Fig. 12) are helpful in visualizing the vertical structure of the tracer distributions and for examining their important northward variations. The ones shown are for a longitude 25° east of the western boundary near the middle of the basin. The diagrams are broken at 1 000 m and plotted on two depth scales to better show the detail in both the shallow and the deep regions.

The temperature section contains several features that are similar to sections in the major ocean basins: a warm thin layer at low and mid-latitudes, a thermocline which is less deep at the equator than at middle latitudes, and a deep, rather homogeneous region below 1 000 m filled with cold water which sinks at high latitudes. However, the thermocline depth at the equator is still too large compared with its depth at higher latitudes and the deep water is

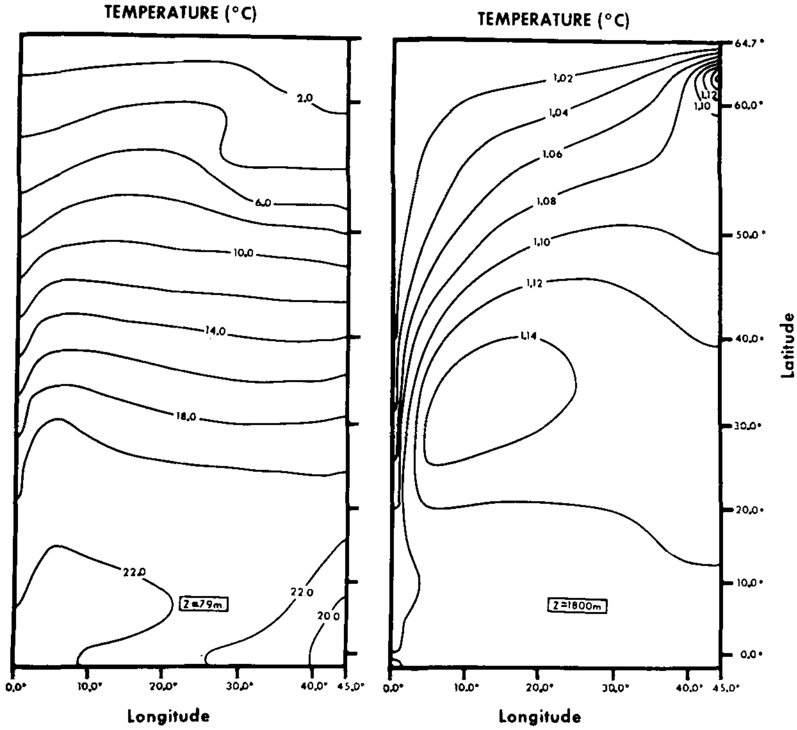

Fig. 8. The temperature distribution at two depths, 79 and 1 800 m.

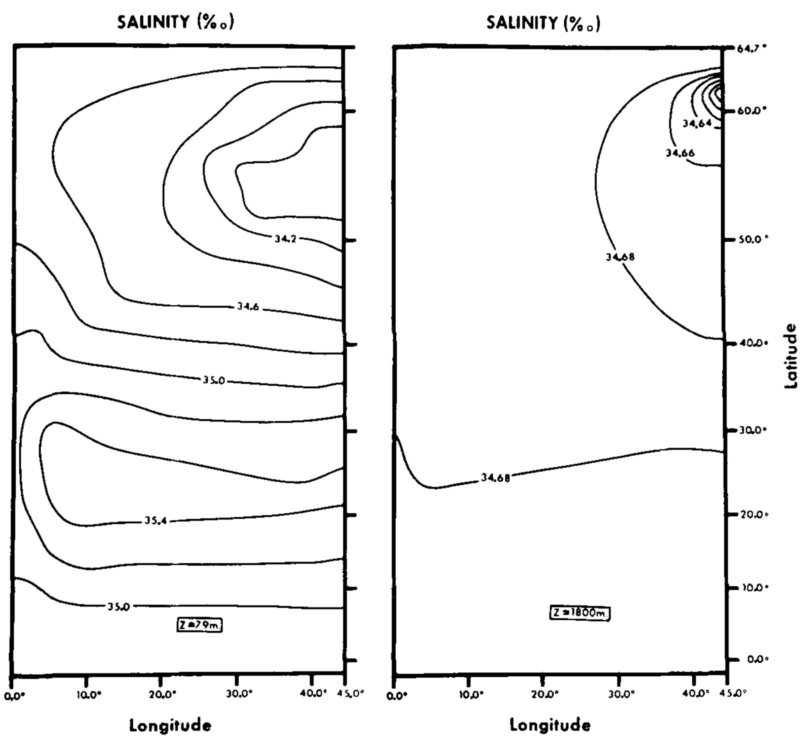

Fig. 9. The salinity distribution at two depths, 79 and 1 800 m.

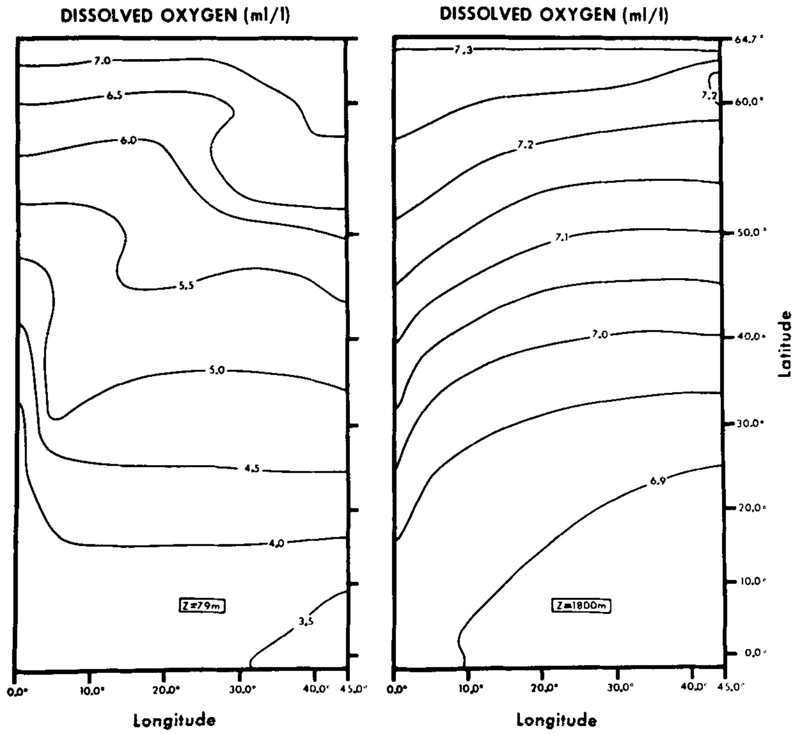

Fig. 10. The distribution of dissolved oxygen at two depths, 79 and 1 800 m. The units are ml/l.

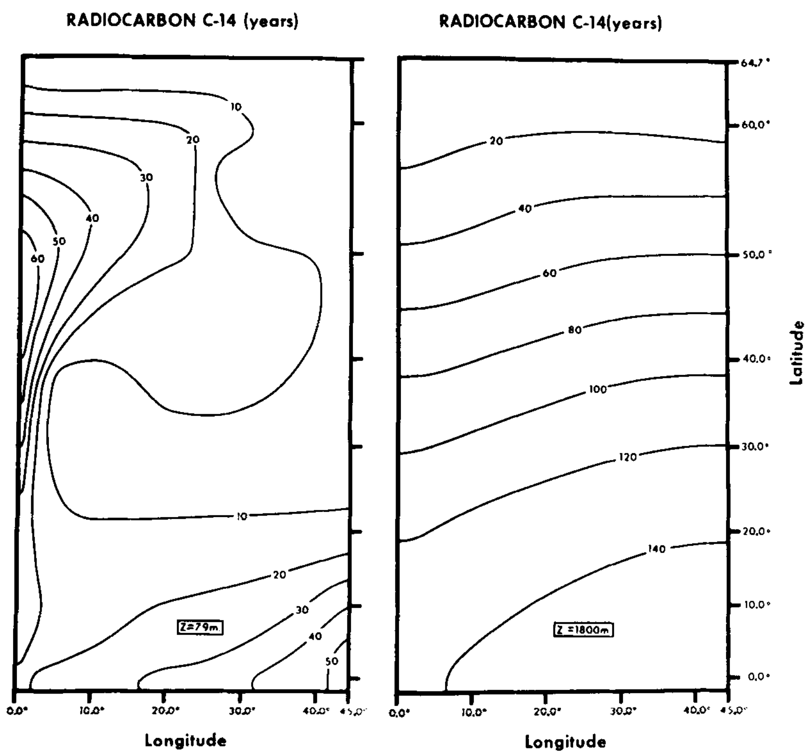

Fig. 11. The distribution of age of the water based upon radiocarbon concentration relative to the surface concentration. The units are years of age.

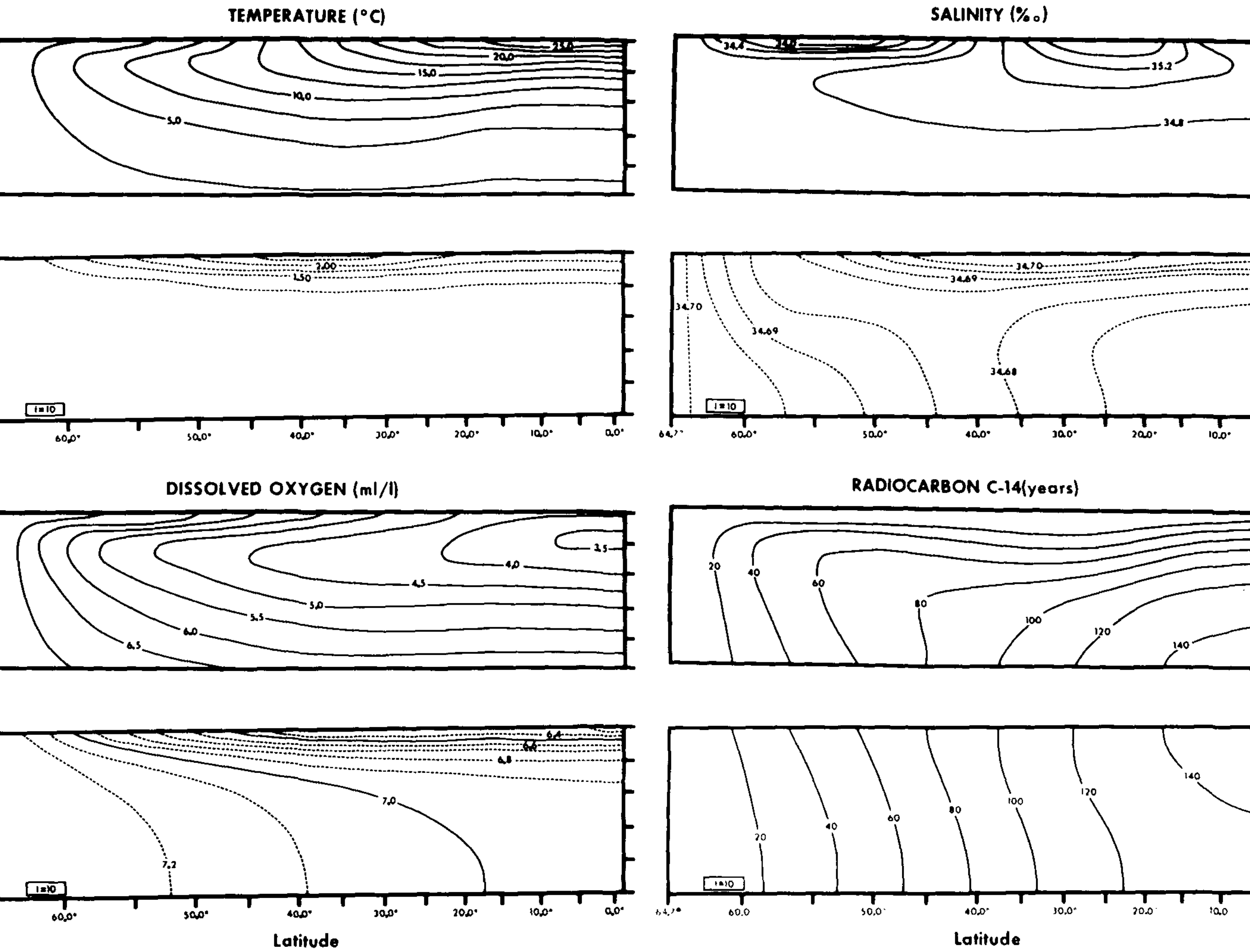

g. 12. Meridional sections of temperature (°C), salinity (°/$_{00}$), oxygen (ml/l), and radiocarbon age (yeasr)at a mid-ocean longitude. Not
rtical scale at 1 000 m and the changes in contour intervalused to bring out detail.

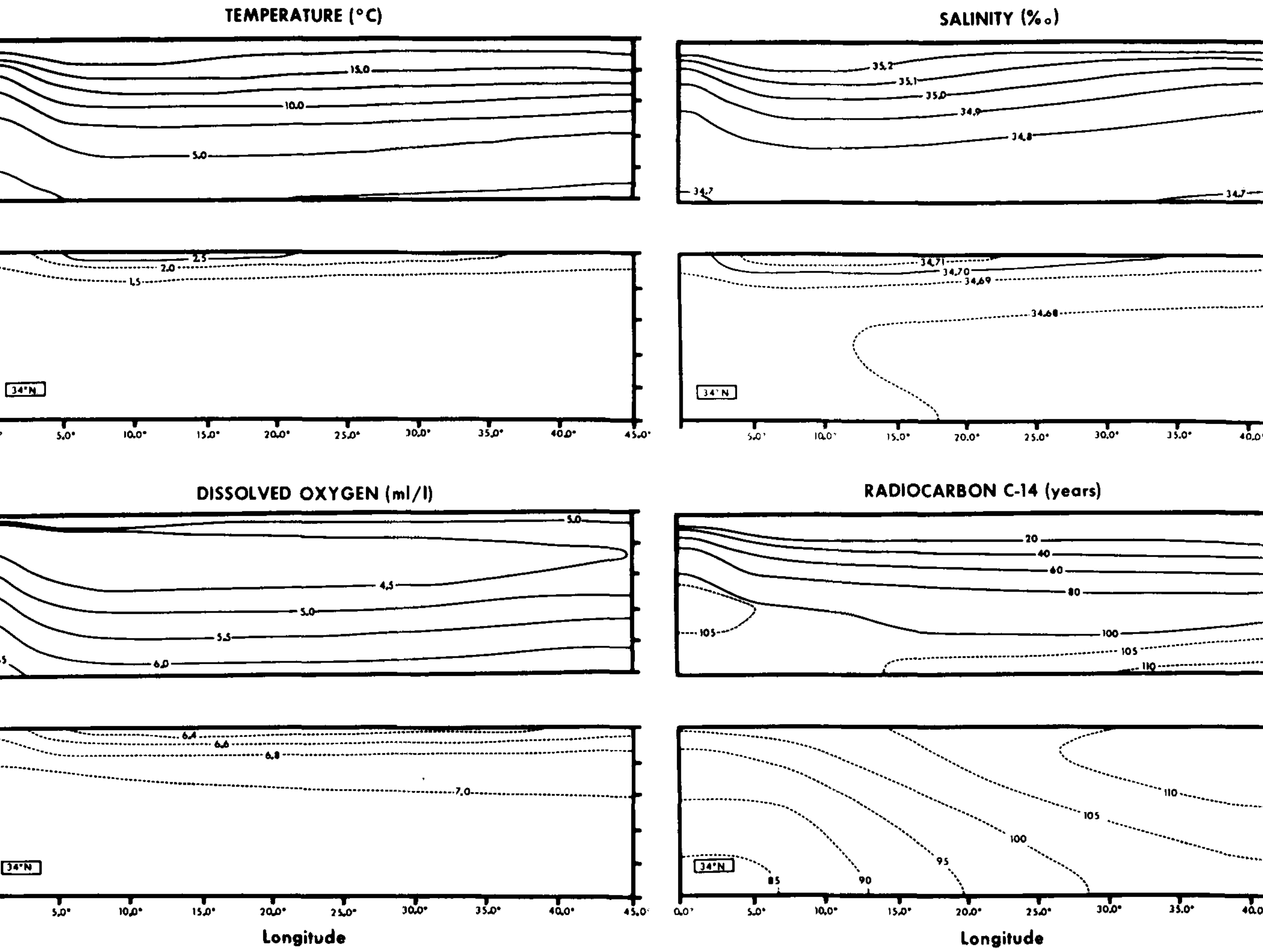

. *13.* Zonal sections of temperature (°C), salinity (°/₀₀), oxygen (ml/l), and radiocarbon age (years) at latitude 34° N. At this latitu
ndary current flows northward above 1 000 m and southward, as an undercurrent, in the deep water.

far too homogeneous, the range of temperature below 2 000 m being only 0.25°C. This homogeneous nature of the deep sea will be discussed in the next section. One further feature of this section that should be pointed out is the temperature inversion which exists above 200 m at high latitudes. The density of the relatively cold surface water is lower than that below because of the pool of relatively fresh water which exists near the surface.

In the salinity section, a high salinity region exists at mid-latitudes (about 25°N) and a low salinity region at high latitudes (55°N). Near the surface these kinds of water are present due to the surface boundary conditions discussed in section 2 and a comparison with real distributions cannot be made because of the difficulties noted there. In fact the Atlantic, Pacific, and Indian Oceans are all quite asymmetric about the equator with respect to salinity and a realistic treatment will require a more complex model than was thought worthwhile in this preliminary calculation. With these reservations it is still of interest to note that salt enters the deep ocean by sinking and by convective mixing near the northern boundary (where at the surface the most dense water is formed: $T = 1.0°C$; $S = 34.70$ ‰) and that some fresher water sinks near the northeast corner. These two processes, in equilibrium with the downward diffusion from the salty surface water at low latitudes, result in a very homogeneous deep ocean with salinities between 34.67 ‰ and 34.70 ‰.

The oxygen section in Fig. 12 has a vertical structure much like that found in the Atlantic basin. The surface is saturated with oxygen but at 200–400 m depth there is an oxygen minimum that can be traced to quite high latitudes. The minimum concentration near the equator is 3.4 ml/l and occurs at about the right depth. Below 2 000 m the water has a very high oxygen content, replenished by advection and convective mixing at high latitudes. The north to south decrease is smaller than that observed in the deep Atlantic; again some factor or combination of factors is producing deep water that is more homogeneous than observed.

The C^{14} results are also illustrated in Fig. 12. "New" water is found at the sea surface and at depth at the northern end of the basin where it sinks and mixes rapidly to the bottom. In the deep water the age increases with distance southward, reaching a maximum age of about 150 years at the equator. This may be compared with an age of 700 years for the North Atlantic Deep Water below 2 500 m (Broecker et al., 1960). Note that this calculation predicts the oldest water to occur at the relatively shallow depth of 1 600 m at this longitude. At greater depths newer water is found.

East–west sections also reveal some interesting structure in the tracer distributions. Fig. 13 shows these distributions at 34° N latitude in the basin. The T and S fields have the characteristic downward tilt of the isolines from east to west over much of the basin and the rapid upward tilt in the region of the western boundary current. The dissolved oxygen at 34° N shows a pronounced minimum centered at 300 m, an upward tilt to the isolines in the upwelling region near the western boundary, and the quite high concentrations in the deep ocean. The last section in Fig. 13 and the section of Fig. 14 show east–west distributions of radiocarbon ages at two latitudes, 34° N and the equator respectively. The structure is interesting in that much is revealed about the pattern of motion in the model as well as the modes of transport of the tracers in the north–south direction. At 34° N a relative minimum age of 84 years is found in the deep water in the southward flowing boundary current on the west side of the basin. The maximum age at this latitude is 115 years at 1 500 m depth adjacent to the eastern boundary. In the equatorial section the age of the western deep water is less than 130 years while the water of maximum age is found again at the relatively shallow depth of 1 500 m near the eastern boundary.

This completes the descriptive picture of the four tracer distributions. Qualitatively the patterns which emerge indicate that many prominent features found in the oceans also occur in the model and it should be fruitful to make calculations which will allow detailed quantitative comparisons with distributions in real ocean basins. Before that can be done however it is necessary to pin down more closely the values of the eddy parameters which give the most realistic predictions of the tracer distributions. Since the resulting distributions depend on these parameters as well as the boundary conditions it is useful to examine how the results of this first calculation depend upon these factors. In particular it is useful to clarify the situation with respect to the very homo-

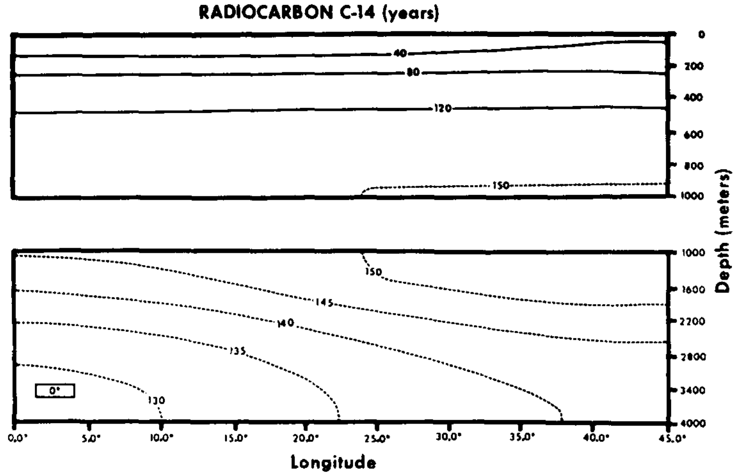

Fig. 14. A zonal section of radiocarbon age (years) at the equator. The oldest water, about 150 years old, is found near the eastern side of the basin at a depth of 1 400 m. Note that the western boundary undercurrent brings newer water all the way to the equator from high latitudes.

geneous deep water and to examine the nature of other discrepancies which cannot be accounted for on the basis of obvious simplifications in geometry and boundary conditions.

5. Salt and heat transports

Let us now make some quantitative comparisons between the model and the ocean which will help make clear the role played by the surface boundary conditions. Two of the important predictions by the model which may be compared with observations are the northward fluxes of salt and heat by the ocean. These may be described alternatively in terms of the zonally averaged evaporation minus precipitation pattern and the zonally averaged heat flux through the sea surface required to account for the salt and heat balance in the surface ocean. Fig. 15 shows for comparison the salt flux found in the model (solid line) and the observed latitudinal distribution of evaporation minus precipitation compiled by Wüst for the oceans of the northern hemisphere (Table 87, p. 226 in Defant's *Physical Oceanography, 1961*). Fig. 16 shows the zonally averaged heat flux into the model ocean as a function of latitude (solid line) and the observed mean annual heat flux for all oceans computed by Emig (1967) from Budyko's atlas (dashed line).

Consider the salt flux curve first. The physical meaning of a flux of salt across the sea surface needs some explanation. The salinity balance at the sea surface is treated implicitly by considering an excess of evaporation over precipitation as a salt source and an excess of precipitation over evaporation as a salt sink. Thus a salt flux is actually a small fresh water flux in the opposite direction. The transports associated with this fresh water flux are several orders of magnitude smaller than those due to other driving effects and can be neglected except in so far as they contribute to changes in salinity.

The two scales in Fig. 15 show the relationship between the magnitudes of the implicit salt flux and the actual evaporation minus precipitation. The magnitudes and shapes of the observed and predicted distributions are reasonably similar considering obvious simplifications in the model. At high latitudes, however, between 55° and 60° N, there is a large salt flux out of the model ocean ($E < P$ there) and next to the northern boundary the flux changes sign so that there exists a thin region of very large flux of salt into the ocean ($E > P$). This behavior is not realistic and the reasons must be sought.

Similar comments apply to the heat flux curves shown in Fig. 16. The flux is the right order of magnitude, about 1×10^{-3} cal cm^{-2} sec^{-1} at low latitudes, but a major dicrepancy occurs near the northern boundary where there is a

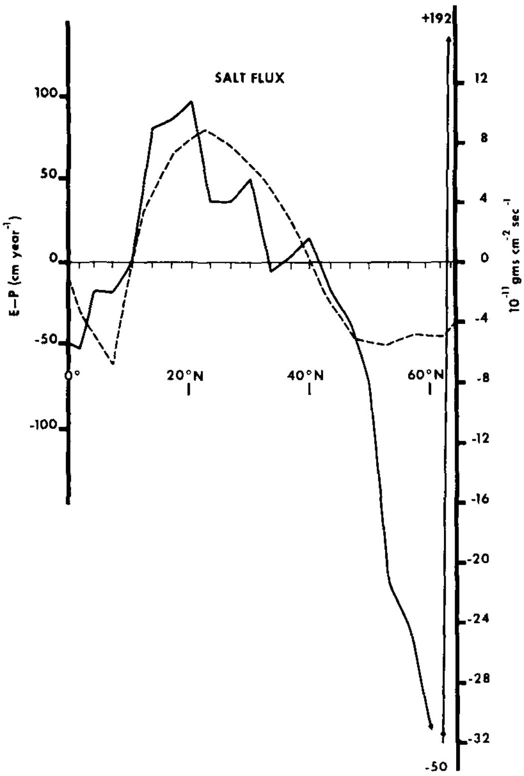

Fig. 15. The zonally averaged salt flux (E–P) into the ocean. The solid curve shows the salt flux predicted by the model and the dashed curve shows the flux based upon evaporation minus precipitation observations for the real ocean. A salt flux out of the ocean in the model is actually a fresh water input ($P > E$). The two scales indicate the relationship between (E–P) and salt flux. Note that the predicted curve goes off scale near the northern boundary.

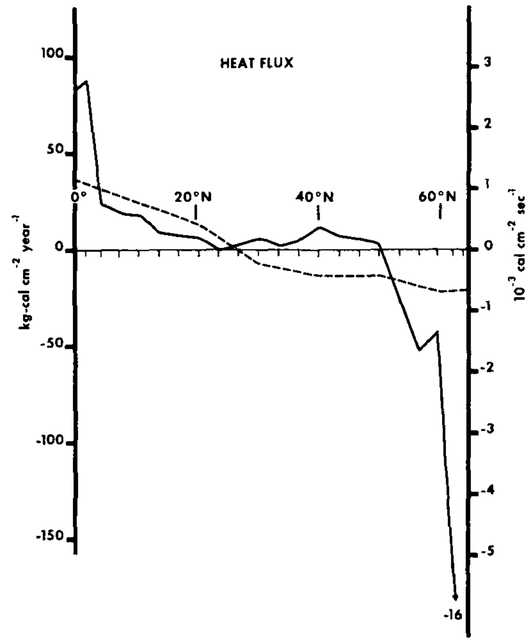

Fig. 16. The zonally averaged heat flux into the ocean. The solid curve shows the heat flux distribution predicted by the model; the dashed curve shows the heat flux distribution computed by Emig (1967) from observations. Note that the predicted curve goes off scale near the northern boundary.

very large flux of heat out of the model ocean. The numbers suggest a factor of 20 error in the thin region near the northern wall. The observed data show a flux reversal latitude (north of which the ocean is cooled and south of which it is heated) at about 27° N whereas the model flux into the ocean is small but positive up to 50° N. This discrepancy, however, is related to the difficulties near the northern boundary since the requirement in the steady state that the total heat entering the basin equals that leaving will lead to a readjustment at lower latitudes if the very large heat flux near the northern boundary was not present.

In general, the model predicts reasonably well the north–south distributions of salt and heat flux except at high latitudes where there are considerable discrepancies. At these latitudes, especially near the northern boundary where the highest density water in the basin is formed at the sea surface, there is considerable vertical mixing associated with a tendency for the water column to become unstable. As a result, the deep ocean at these latitudes is in rapid communication with the surface and plays an important role in determining the surface fluxes. Thus the abyssal ocean must be examined to understand the nature of the difficulty.

Consider then the abyssal time scales that are found in our calculation. The source of deep water in the northeast corner of the basin has a strength of 17×10^6 m^3/sec while the volume of the deep sea ($> 1\,000$ m) is 8.6×10^7 km^3. Thus the deep water is renewed by advective processes about every 150 years. This is cloxe to the value suggested by the model radiocarbon data. However it might have been expected that, since part of the deep sea is bypassed by the

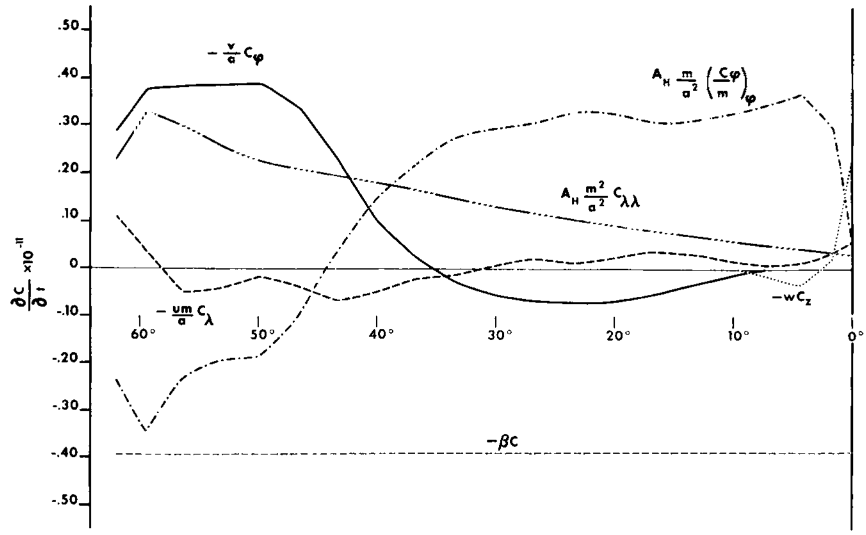

Fig. 17. The balance of terms in the deep sea. The various terms in the radiocarbon equation, computed at a depth of 3 000 m and at a mid-ocean longitude, are shown as a function of latitude. The local time rate of change C_t and the vertical diffusion KC_{zz} are to small to be shown on this scale.

swift boundary currents, some interior regions would have even older water. This would imply a more realistic variation in the deep tracer distributions. A calculation of the time scales for diffusive processes clarifies the situation. The time scales for vertical and horizontal diffusion, estimated from H^2/K and L^2/A_H respectively, are 4 400 years and 150 years. Here H and L are the depth and width of the ocean, and K and A_H are the vertical and horizontal eddy diffusivities for the tracers. The short time scale for horizontal diffusion (the same size as the advective time scale) suggests that the distribution of properties away from the western boundary is governed by rapid horizontal diffusion.

This is confirmed by examining the balance of terms in the radiocarbon equation at a mid-ocean longitude and a depth of 3 000 m (Fig. 17). Six terms contributing to the local time rate of change in radiocarbon concentration are shown as a function of latitude. Two others, the vertical diffusion term KC_{zz} and the local rate of change C_t, are too small to show up on the graph. In general the local rate of radioactive decay is balanced by an input from several terms, but at low latitudes (5° N to 40° N) the major term is southward diffusion while at high latitudes the southward advection of radiocarbon is the largest balancing tendency. There is an important contribution from the other lateral diffusion term, the eastward diffusion of radiocarbon out of the western boundary current. At the equator vertical advection is important locally. This is the only place in the deep interior where vertical processes play a significant role, other than in the convecting region adjacent to the northern boundary and in the region adjacent to the western boundary. This analysis shows that in the model abyssal ocean advective processes and horizontal diffusion dominate. This coupled with the rapid convective mixing at the northern boundary, leads to a deep sea that is quite homogeneous, with tracer values close to their imposed surface values at the northern boundary. Furthermore the discrepancy in the fluxes out of the basin near the northern boundary is now explained. The large horizontal diffusion of heat and salt in the deep sea leads to a large destabilizing tendency and hence to a strong vertical mixing near the northern wall. The surface fluxes must be overly large there to accommodate this behavior.

The changes in the model necessary to establish more realistic distributions are easily incorporated in future studies of the abyssal ocean and the distribution of properties in the sea. First, it would seem better to impose as the surface boundary conditions the fluxes of temperature and salinity (and perhaps other tracers as well) rather than the surface values themselves. This would lead to an ocean in which the destabilizing tendency at high latitudes, caused by the balance between the efflux of heat and the excess of precipitation over evaporation there, is determined by observations, and the vertical mixing would be correspondingly more realistic. Secondly, to achieve time scales in the model like those observed in the deep ocean, the horizontal eddy diffusivity A_H (equal to 5×10^7 cm^2/sec in this study) must be reduced by a factor of 5 to 10. Recent results of Kuo & Veronis (1970) in a much simpler model suggest the same conclusion: the horizontal eddy diffusivity must be 1×10^7 cm^2/sec or less in order to achieve realistic horizontal distributions of oxygen and radiocarbon in the deep ocean. It is not clear how the vertical structure of the distributions will be changed by these modifications however. Whether for example the interior will begin to show a Munk (1966) kind of vertical balance of terms or whether, as in this case, horizontal processes still tend to dominate remains to be seen. It will be necessary to carry out a variety of experiments to delimit the various kinds of balance of terms which can take place. In any case the two modifications mentioned above are likely to enhance the realism of the model, and it will be of interest to examine how the *patterns of motion* found here are altered by these changes. A study of this kind is underway.

6. Conclusions and future experimentation

This preliminary experiment has been carried out to examine the possibility of using tracer distributions to study the general circulation of the ocean and to investigate the role of diffusive and advective processes in establishing these distributions in the deep sea. The results suggest that a model of this kind is capable of simulating quite realistic distributions of properties and, with improvements in the model suggested by this study and by future ones, should be able eventually to compute the transports by oceanic motions of heat, salt, and other chemical constituents throughout the ocean. It would seem worthwhile therefore to continue development of the model by exploring a variety of sizes of eddy diffusion parameters and a variety of boundary conditions in order to achieve the most realistic simulation possible.

Despite the gross similarities between ocean and model, however, it is still not clear whether all of the various water masses found in the world ocean are determinable by simply satisfying the proper boundary conditions, using a better choice of eddy coefficients, and putting in the geometric complexities. It may be necessary to make some important modifications to the internal physics, for example by considering different convective adjustment or eddy diffusion hypotheses. It may also be necessary to examine inherently time-dependent systems such as seasonal or even long term variations in the heating–cooling and the evaporation–precipitation patterns. These and similar considerations will have to be looked into during the development stages of the model.

Although more basic experimentation is the first order of business, a longer range goal is to use such a model as this one to quantitatively reproduce the distribution of properties in the world ocean. This will provide a test for the validity of the three-dimensional ocean circulation patterns computed by the model which at present cannot be vertified in any other way. Moreover such distributions will allow classical examinations of the model data, for example T-S frequency diagrams, isentropic analyses of the data, and various kinds of budget calculations, with which similar ocean data can be compared. These studies will provide an important link between the theoretical ideas inherent in the numerical experiment and the complexities of the descriptive data.

The inclusion of additional tracers will provide valuable new tests for the model. The GEOSECS program, an ambitious plan by the geochemists to measure a whole host of chemical species in detailed north–south sections in the ocean (hence Geochemical Ocean Sections), will obtain data which can usefully be incorporated into such a model. These data will put further constraints on the validity of the dynamical solution, but in addition the tracer model should be a useful framework for looking at the data from the geochemist's point of view. It should be possible to use the observed distributions of some of the chemical constituents to predict the internal source-sink terms $R(s)$ for these quantities, knowing the advection and diffusion characteristics required to faithfully reproduce temperature and salinity distributions. This will allow the geochemist to evaluate the local chemistry and/or the particulate fluxes that are responsible for these internal sources and sinks.

Finally it should be mentioned that the tracer model will provide a valuable tool in pollution management, particularly with regard to the disposal and dispersal in the ocean of various unwanted substances. The ocean acts as a sink for many man-made pollutants, including the products of nuclear fission, chemical fuel combustion, and other wastes such as pesticides. A model which can successfully simulate the observed distributions of various chemical species can be put to work finding the pathways by which pollutants travel into the ocean and can help to develop an understanding of the capacity of the ocean to absorb them.

REFERENCES

Arons, A. B. & Stommel, H. 1967. On the abyssal circulation of the world ocean. III. An advective lateral mixing model of the distribution of a tracer property in an ocean basin. *Deep Sea Res. 14*, 441–457.

Bien, G. S., Rakestraw, N. W. & Suess, H. E. 1965. Radiocarbon in the Pacific and Indian Oceans and its relation to deep water movements. *Limnol. Oceanogr. 10*, (Suppl), R25–R37.

Bolin, B. & Stommel, H. 1961. On the abyssal circulation of the world ocean. IV. Origin and rate of circulation of deep waters as determined with aid of tracers. *Deep Sea Res. 8*, 95–110.

Broecker, W. S., Gerard, R., Ewing, M. & Heezen, B. C. 1960. Natural radiocarbon in the Atlantic Ocean. *J. Geophys. Res. 65*, 2903–2931.

Bryan, K. 1969. A numerical method for the study of ocean circulation. *J. Computat. Phys. 4*, 347–376.

Bryan, K. & Cox, M. D. 1967. A numerical investigation of the oceanic general circulation. *Tellus 19*, 54–80.

Bryan, K. & Cox, M. D. 1968. A nonlinear model of an ocean driven by wind and differential heating, parts I and II. *J. Atmos. Sci. 25*, 945–978.

Craig, H. 1957. The natural distribution of radiocarbon and the exchange time of carbon dioxide between atmosphere and sea. *Tellus 9*, 1–17.

Craig, H. 1969. Abyssal carbon and radiocarbon in the Pacific. *J. Geophys. Res. 74*, 5491–5506.

Defant, A. 1961. *Physical Oceanography*. Pergamon Press, 729 pp.

Eckart, C. 1958. Properties of water, part III. *Amer. J. Sci. 256*, 225–240.

Emig, M. 1967. Heat transport by ocean currents. *J. Geophys. Res. 72*, 2519–2529.

Keeling, C. D. & Bolin, B. 1967. The simultaneous use of chemical tracers in ocean studies. I. General theory of reservoir models. *Tellus 19*, 566–581.

Keeling, C. D. & Bolin, B. 1968. The simultaneous use of chemical tracers in oceanic studies. II. A three-reservoir model of the North and South Pacific oceans. *Tellus 20*, 17–54.

Kuo, H. & Veronis, G. 1970. Distribution of tracers in the deep oceans of the world. *Deep Sea Res. 17*, 29–46.

Munk, W. H. 1950, On the wind-driven ocean circulation. *J. Mat. 7*, 79–93.

Munk, W. H. 1966. Abyssal recipes. *Deep Sea Res. 13*, 707–730.

Riley, G. A. 1951. Oxygen, phosphate, and nitrate in the Atlantic Ocean. *Bull. Bingham Oceanogr. Coll. 13*, 1–126.

Saint-Guily, B. 1956. Sur la théorie des courants marins induits par le vent. *Ann. Inst. Ocean.* (Paris), *33*, 1–64.

Stommel, H. 1957. A survey of ocean current theory. *Deep Sea Res.* 4, 149–184.

Stommel, H. 1958. The abyssal circulation. *Deep Sea Res. 5*, 80–82.

Stommel, H. & Arons, A. B. 1960. On the abyssal circulation of the world ocean. I. Stationary planetary flow patterns on a sphere. *Deep Sea Res. 6*, 140–154.

Sverdrup, H. U. & Fleming, R. H. 1941. The waters off the coast of southern California. March to July, 1937. *Scripps Inst. Oceanogr. Bull. 4*, 261–378.

Sverdrup, H. U., Johnson, M. W. & Fleming, R. H. 1942. *The Oceans: their physics, chemistry and general biology*. Prentice-Hall, Englewood Cliffs, N. J., 1087 pp.

Sverdrup, H. U. 1947. Wind-driven currents in a baroclinic ocean; with application to the equatorial currents of the Eastern Pacific. *Proc. Natl. Acad. Sci.* (USA) *33*, 318–326.

Swallow, J. C. & Worthington, L. V. 1961. An observation of a deep counter current in the western North Atlantic. *Deep Sea Res. 8*, 1–19.

Todd, J. 1962. *Survey of numerical analysis*. McGraw-Hill, New York, 589 pp.

Veronis, G. 1966. Wind-driven ocean circulation. Part 2. Numerical solutions of the non-linear problem. *Deep Sea Res. 13*, 31–55.

Wyrtki, K. 1962. The oxygen minimum in relation to ocean circulation. *Deep Sea Res. 9*, 11–28.

РАСПРЕДЕЛЕНИЕ ОКЕАНСКИХ ТРАССЕРОВ. ЧАСТЬ I. ПРЕДВАРИТЕЛЬНЫЙ ЧИСЛЕННЫЙ ЭКСПЕРИМЕНТ

Для определения трехмерных распределений растворенных кислорода и радиоуглерода и полей температуры, солености и скорости в океане, приводимом в движение ветром и термохалинными процессами, был приведен численный эксперимент. Целью этих предварительных вычислений была проверка полезности трассерной модели для изучения происхождений водных масс и создание основы для дальнейшего исследования природы источников, возраста и циркуляции глубоководных океанических масс. Многое из наших знаний о характере циркуляции и перемешивания в океане было почерпнуто из рассмотрения распределений характеристик с помощью упрощенных одномерных и двумерных моделей. В данной работе исследование трассеров распространяется на три измерения с помощью численной модели океанической циркуляции типа, описанного Брайеном (1969). С набором заданных параметров, уравнений и граничных условий, определяющих модель океана, произведены предсказания распределений четырех «трассеров» — температуры, солености, растворенных кислорода и радиоуглерода, также как и структуры циркуляции. На основе этого первого эксперимента можно сделать некоторые важные выводы в отношении тех особенностей, которые необходимы в любой модели для удовлетворительного учета наблюдаемых распределений.

В I части описана физическая модель и ее численный аналог, а также расчетная техника, используемая для определения стационарного состояния. Результаты эксперимента со значениями коэффициентов турбулентного перемешивания $K = 1$ *см*²/сек (по вертикали) и $A_H = 5 \cdot 10^7$ *см*²/сек (по горизонтали) обсуждаются довольно подробно с целью понять временные масштабы для глубокого моря, а также и для более мелководных областей. Структупа потока и распределения четырех трассеров связываются друг с другом путем определения ролей диффузии, адвекции и затухания в модели. Делается сравнение между наблюдаемыми и вычисляемыми на поверхности потоками тепла и испаряемой минус осаждаемой влаги, чтобы установить влияние граничных условий на характер распределений. Эти результаты указывают, в каком направлении следует вести дальнейшие исследования в конструировании реалистических моделей океана. Проводятся вычисления с меньшими значениями коэффициентов турбулентного перемешивания и с другими граничными условиями, результаты которых будут описаны во II части.